UNIVERSITY OF BIRMINGHAM

Different photo-catalytic degradation of methylene blue by varied ZnO nanorods on dissimilar stainless steel wire sieves

Jing, Weixuan; Cheng, Yanyan; Gao, Weizhou; Jiang, Zhuangde; Jiang, Kyle; Shi, Jiafan; Zhou, Fan

Document Version
Peer reviewed version

Link to publication on Research at Birmingham portal

Accepted Manuscript

Different photo-catalytic degradation of methylene blue by varied ZnO nanorods on dissimilar stainless steel wire sieves

Weixuan Jing[*a], Yanyan Cheng[a], Weizhou Gao[a], Zhuangde Jiang[a], Kyle Jiang[b], Jiafan Shi[a], Fan Zhou[a]

[a]*State Key Laboratory for Manufacturing Systems Engineering at Xi'an Jiaotong University, Xi'an 710049, China*

[b]*School of Mechanical Engineering, University of Birmingham, Birmingham B15 2TT, UK*

[*]Corresponding author. Tel.: +86-29 82668616
E-mail address: wxjing@mail.xjtu.edu.cn (W.X. Jing)

Graphical abstract

ZnONRs on SSWs of different diameters

Different surface morphologies of corresponding SSW-supported ZnONRs

Different photo-degradation of methylene blue by related SSW sieve-supported ZnONRs
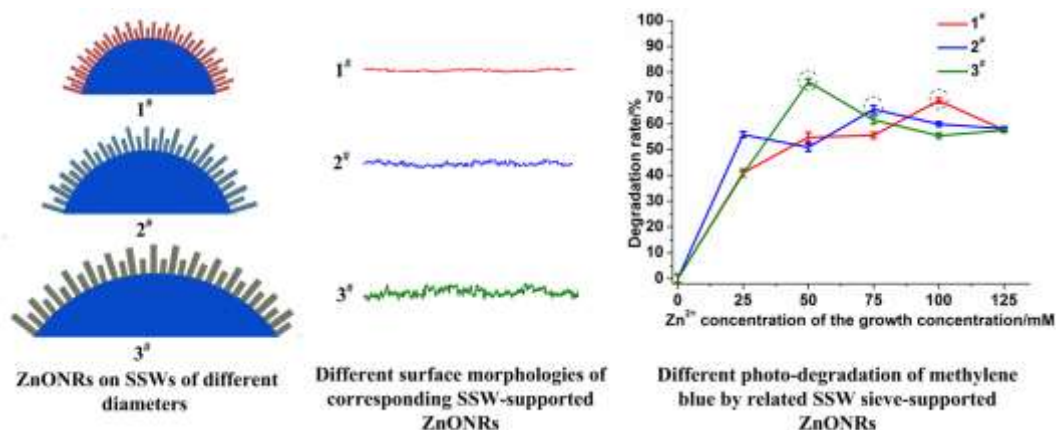
Highlights

- Varied ZnONRs were hydrothermally synthesized on SSW sieves of different meshes.

- Synthesizing parameters and SSW diameters affect surface morphologies of SSW-supported ZnONRs.

- Surface morphology and mesh size influence wettability of SSW sieve-supported ZnONRs.

- Surface morphology and wettability decide MB degradation of SSW sieve-supported ZnONRs.

ABSTRACT: Methylene blue (MB) was degraded via ultraviolet (UV) irradiation by ZnO nanorods (ZnONRs) which were hydrothermally synthesized on stainless steel wire (SSW) sieves of different meshes. It was found that besides synthesizing parameters, the diameter of a SSW also affected the nucleation density of ZnO seeds and the size of diffuse zone of Zn^{2+} and O^{2-} ions, and thus the surface morphology of

the SSW-supported ZnONRs. The surface morphology of SSW-supported ZnONRs, together with the mesh size of a SSW sieve, further influenced significantly the wettability of the SSW sieve-supported ZnONRs. Of all three groups of SSW sieve-supported ZnONRs, those with Gaussian random rough surfaces are most hydrophilic, hence the actual contacting surface areas of (001) active crystal planes of ZnONRs with MB solution are the largest, the yield of hydroxyl radicals the highest, and eventually the photo-catalytic degradation of MB the optimal.

Keywords ： A. Semiconductors; B. Solvothermal; C. Electron microscopy; D. Catalytic properties; D. Surface properties

1. Introduction

Photo-catalytic degradation has been widely used to de-color and clean various synthetic organic dyes in wastewater, for instance, MB, methylene orange, rhodamine B, azo dye, and methanol, and is essential for the environmental sustainability of textile, leather, paint, food, plastic, and cosmetic industries [1]. Of semiconductor metal oxides and sulfides including TiO_2, ZnO, WO_3, CdS, and ZnS, nanostructured ZnO is more attractive as a catalyst due to its suitable band gap, considerable photo-catalytic efficiency of various polluted effluents, and more important, neutral solution in which related catalyzing reaction is conducted [2-4]. In comparison with powdery form of this catalyst, ZnONRs synthesized on a certain substrate can not only avoid catalyst aggregation, but also benefit adsorption of reactants upon the

catalyst and separation of the catalyst from reaction medium, and thus give rise to higher photo-catalytic degradation efficiency of a specific organic pollutant [5]. A wide variety of substrates on which corresponding catalysts are deposited have been used in literatures, such as indium tin oxide glass [6], copper plate [7], silica [8], crystal or polyster film [9], polyethylene fiber [10], SSW [11] and nylon [12] sieves etc. By contrast with other substrates, a SSW sieve is more frequently employed thanks to its extensive surface area, efficient mass and heat transfer, lower pressure drop, lightweight, flexibility, and low cost. For instance, Lu used the direct electro-deposition method to prepare the arrays of well-aligned single-crystalline ZnO nanorods on SSW sieves, and investigated the detailed effects of the electrochemical parameters on the orientation, lengths, average diameter, and density of the ZnO nanorods and further on the photo-degradation of rhodamine B [13]. Vu hydrothermally synthesized ZnONRs on SSW sieves under several different conditions, and discussed the effects of the synthesizing parameters on the quantum yield, morphologies, lengths, and widths of the ZnO nanorods as well as on the photo-degradation of MB solution under UV irradiation [5, 14, 15]. Jung used the photochemical deposition method and deposited flower-like CuO nanostructures on the as-synthesized ZnO nanorods to obtain heterostructured CuO-ZnO nanorods on SSW sieves, then quantitatively characterized the diameters and lengths of the ZnO nanorods and qualitatively the CuO-ZnO heterostructures, and further discussed the effects of multilayer sieves, dual light source, and pH values of the precursor solution on the photo-degradation of azo dye [16]. Marbán hydrothermally synthesized

4

Cu/Co-structured catalysts on SSW sieves, and studied the effects of Cu content and calcination temperature on the crystal sizes of the Cu/Co nanostructures and average diameters of the pores to improve the spinel yield, the specific surface area, and further the methanol decomposition [17].

Nevertheless, aforementioned literatures demonstrate apparent disadvantages as follows. Firstly, although these SSW-supported nanostructured catalysts often form random rough surfaces, their profiles were not extracted from related SEM micrographs and the characteristic parameters of the surface morphologies were not acquired. Instead, in most cases only SEM-based direct measurement route was employed and limited geometrical parameters such as diameter, length, density, and orientation of the catalysts were obtained, therefore the surface morphologies of these SSW-supported catalysts were merely approximately characterized. Secondly, the detailed effect of the surface morphologies on the wettability of aforementioned SSW sieve-supported catalysts was not investigated, thus the sizes of air bubbles trapped within the screen openings of the catalyst-deposited SSW sieves were not evaluated, and the total actual contacting surface area of the catalysts with solution of specific organic pollutant were not discussed. These two disadvantages hinder the fine regulation of related fabrication processes and further the performance improvement of corresponding ZnONR-based photo-reactors.

In this paper ZnONR-deposited SSW sieves of different meshes were batch fabricated. The effects of Zn^{2+} concentration of the growth solution and diameters of the SSWs on the surface morphologies and the wettability of these ZnONR-coated

SSW sieves were investigated, and thus the photo-catalytic degradation of MB by the ZnONR-based photo-reactors was optimized.

2. Experimental details

2.1. Materials and apparatus

Absolute ethyl alcohol, anhydrous zinc acetate (Kemiou Chemical Reagent Factory, China), sodium hydrate (Hedong Red Cliff Chemical Reagent Factory, China), zinc nitrate, hexamethylenetetramine, six hydrated zinc nitrate, MB solution (Tianjin Fuchen Chemical Reagents Factory, China) are all analytical reagents. DI-water (18.25 MΩ·cm) and SSW sieves of meshes 300, 200, and 150 (Outokumpu Stainless, USA) were used.

Electronic balance (FA1004N, Changzhou Xingyun Electronic Equipment Co. Ltd., China), water-bath (DK-98-IIA, Tasite, China), drying oven (DZF-6020, Shanghai Yiheng Technical Co. Ltd., China), magnetic stirrer (BII-3，Shanghai Sile Automation Science & Technology Co. Ltd., China), ultrasonic washer (KQ-100DE, Kunshan Ultrasonic Instruments Co. Ltd., China), SEM (SU8010, Hitachi, Japan), confocal microscopy (OLS4000, Olympus Corporation, Japan), X-ray diffractometer (XRD, TCM4400, PANalytical Holland), Fourier transform infrared (FT-IR) spectrometer (TENSOR27, Bruker, Germany), contact angle (CA) meter (OCA20, Dataphysics company, Germany), UV analyzer (ZF-20D, Xi'an Yuhui instrument Co. Ltd., China), and UV-visible spectrophotometer (UV-3600, Shimadzu Corporation) were employed.

2.2. Hydrothermal synthesis of ZnONRs on 1#-3# SSW sieves

As for synthesis of ZnONRs on SSW sieves to photo-degrade different organic pollutants, hydrothermal synthesis [18], chemical vapor deposition [19], thermal evaporation method [20], and pulse laser deposition [21] are frequently employed. Since hydrothermal synthesis not only is cost effective but also delivers ZnONRs of high crystallinity, it was employed in this paper.

SSW sieves of mesh 300, 200, and 150 were cut into several square pieces measuring 1×1 cm^2 and designated as $1^{\#}$, $2^{\#}$, and $3^{\#}$. These square sieves were cleaned in the ultrasonic washer with absolute ethyl alcohol and DI water for 5 min respectively, then in the drying oven dried at 120 °C for 10 min. ZnO seed solution of Zn^{2+} concentration 1 mM was prepared with zinc acetate dihydrate (Zn(CH$_3$COO)$_2$·2H$_2$O), sodium hydrate (NaOH), and absolute ethyl alcohol. Zinc nitrate (Zn(NO$_3$)$_2$·6H$_2$O), hexamethylenetetramine (C$_6$H$_{12}$N$_4$) and DI water were used to produce growth solution of Zn^{2+} concentration 25, 50, 75, 100, and 125 mM. A square sieve of a specific mesh was immersed into the ZnO seed solution for 1 min, and then annealed in the drying oven at 120 °C for 10 min. These immersing and annealing processes were repeated twice more. Then the ZnO seed-coated square sieve was put into the growth solution of a specific Zn^{2+} concentration in a beaker. The beaker was sealed with a preservative film and placed into the water-bath at 90 °C for 2.5 h. Afterwards the sample was taken out and cleaned in the ultrasonic washer with DI water for 5 min, and dried in air.

2.3. Characterization of the ZnONRs on SSW sieves

Based on SEM micrographs and Image Processing Toolbox of MATLAB

software, the profiles of the SSW-supported ZnONRs at front view were extracted. According to these extracted profiles, the characteristic parameters were acquired, and therefore the surface morphologies of the SSW-supported ZnONRs were quantitatively characterized. The characteristic parameters of a random rough surface often include roughness Ra (the fluctuations of surface heights around an average surface height), skewness Sk (the measure of the symmetry of the height distribution about a mean surface level), kurtosis Ku (the measure of the sharpness of the height distribution function) and correlation length ζ (the value of the lag length at which the auto-correlation function drops to 1/e of its value at zero lag) [22].

In addition, the CAs of SSW sieve-supported ZnONRs were acquired with the CA meter, and the volume of a DI water droplet was set to be 5 μL. Using CuKα radiation (λ=1.5418 Å) and operating at 40 kV and 40 mA, the XRD patterns of the ZnONRs were examined at a scanning rate of 8º/min for 2θ ranging from 20º to 80º. The FT-IR spectra of the ZnONRs were obtained within the wavelength rang of 8000-350 cm^{-1}, the main absorption bands were identified, especially that corresponds to O–H modes. The transmittances at the absorption bands of O–H modes were compared among ZnONRs synthesized at different Zn^{2+} concentration of the growth solution on 1$^{\#}$, 2$^{\#}$, and 3$^{\#}$ SSW sieves, and thus the attached hydroxyl radicals were qualitatively evaluated.

2.4. Photo-catalytic degradation of MB with the ZnONRs on SSW sieves

Aforementioned ZnONR-deposited SSW sieves were put into MB solution of concentration 10 mg/L respectively, and then were irradiated by UV light for 2 h in

the UV analyzer with light intensity 6.0×10^3 μW/cm^2. The absorbance of the MB solution was obtained with the UV-visible spectrophotometer at its maximum absorption wavelength 553 nm, and thus the photo-catalytic degradation of MB solution by 1[#]-3[#] SSW sieve-supported ZnONRs via UV irradiation was quantitatively evaluated.

3. Results and discussion

3.1. Characterization of ZnONRs on 1[#]-3[#] SSW sieves

3.1.1. 1[#]-3[#] SSW sieves

The red, blue, and green curves in Fig. 1a-c are the extracted profiles of 1[#]-3[#] SSWs at side view. According to these profiles Ra values of 1[#]-3[#] SSWs at side view are determined to be 59.8, 65.5, and 69.1 nm. With the con-focal microscopy Ra values of the SSWs at front view are acquired to be 80.3, 87.6, and 91.2 nm. Apparently, Ra values at front view are quite larger than corresponding ones at side view. It indicates that the surface textures of these SSWs are anisotropic, and the roughness at front view more greatly affects subsequent hydrothermal synthesis of ZnONRs than the one at side view. Moreover, among 1[#]-3[#] SSWs Ra values either at front or side view change unremarkably. It suggests that the surface textures of 1[#]-3[#] SSWs are very similar to each other, and thus their effects on subsequent hydrothermal synthesis of ZnONRs are quite the same. It concludes that as cylindrical substrates 1[#]-3[#] SSW sieves meet the geometrical requirements for subsequent hydrothermal synthesis of ZnONRs.

3.1.2.   2[#] SSW sieve-supported ZnONRs

Fig. 2a and the top right inset in Fig. 1b demonstrate that in comparison with the bare $2^{\#}$ SSW sieve, the ZnONR-coated one is still uniform. Fig. 2b shows that the ZnONRs are evenly distributed upon the surface of the SSW. The gap between the ZnONRs film and the surface of the SSW is attributed to the SSW deformation during cutting process with a pair of surgical scissors. Fig. 2c and its bottom left inset illustrate in detail that the ZnONRs of high spatial frequency are superimposed on the cylindrical substrate of low spatial frequency, suggesting that the SSW-supported ZnONRs with desirable surface morphology was produced. Fig. 2d exhibits that the hexagonal ZnONRs of high quality are evident and well-aligned.

3.2. Detailed ZnONRs on $1^{\#}$-$3^{\#}$ SSWs

The columns of SEM micrographs in Fig. 3 illustrate the detailed ZnONRs synthesized at different Zn^{2+} concentration of the growth solution on specific SSW sieves. When Zn^{2+} concentration of the growth solution becomes larger, first the diameters of ZnONRs increase (Fig. 3a1-a4; Fig. 3b1-b3; Fig. 3c1-c2), then side-by-side coalescences among neighboring ZnONRs start to occur (Figs. 3a5, 3b4, 3c3), and eventually ZnO nanostructures instead of ZnONRs appear (Figs. 3b5, 3c4-5). Meanwhile the orientation of ZnONRs is first random, then correlated, and finally random to some extent again. In addition, the sizes of the valleys among bundles of neighboring ZnONRs steadily decrease. All these suggest that synthesizing parameters influence significantly the surface morphologies of SSW-supported ZnONRs.

The rows of SEM micrographs in Fig. 3 show the ZnONRs deposited on

different SSWs at specific Zn^{2+} concentration of the growth solution. Obviously, a SSW of larger diameter gives rise to thicker ZnONRs. This is attributed to less density of the ZnO seeds and larger size of the diffusion zone of Zn^{2+} and O^{2-} ions upon the surface of the SSW with larger diameter. Also it is worthy to note that even though corresponding Zn^{2+} concentration of the growth solution are different, the ZnONRs framed in red dashed squares in the 4th, 3rd, and 2nd rows are quite similar to each other. All these indicate again that besides synthesizing parameters, the diameters of SSWs also affect dramatically the surface morphologies of related SSW-supported ZnONRs. Moreover, the ZnONRs in SEM micrographs above the red dashed squares are with sharp tips and quite random orientation whilst those below the red dashed squares are with hexagonal tips and more correlated orientation.

Fig. 4 shows the number densities of ZnO nanorods synthesized at different Zn^{2+} concentration of the growth solution on $1^{\#}$, $2^{\#}$, and $3^{\#}$ SSWs. It demonstrates that when the value of the synthesizing parameter becomes larger, all the densities of ZnONRs on $1^{\#}$, $2^{\#}$, and $3^{\#}$ SSWs first decrease sharply, then reach the related knee points, and finally increase slightly. This indicates that the growth of related ZnONRs on all SSWs was slightly, remarkably, and moderately obstructed by neighboring ones. It is attributed to the Zn^{2+} concentration of the growth solution and the diameters of ZnONRs. Moreover, the average densities of ZnONRs on $1^{\#}$, $2^{\#}$, and $3^{\#}$ SSWs steadily decrease. It suggests that the growth obstruction of ZnONRs by neighboring ones (also including the coalescence with neighboring ZnONRs) on $1^{\#}$, $2^{\#}$, and $3^{\#}$ SSWs gradually diminishes. The curvature radii of the SSWs are ascribed to these different

growth obstructions [23]. That is, the larger the curvature radius of an SSW is, the less radiating the ZnONRs are from the surface of the cylindrical substrate, and thus the more the growth obstruction of ZnONRs by their neighboring ones, and finally the less the density of the as-synthesized ZnONRs. It is also worthy noticing that the least densities of ZnONRs on 1[#], 2[#], and 3[#] SSWs occur at Zn^{2+} concentration 100, 75, and 50 mM of the growth solution respectively, coinciding with the ones at which the Gaussian random rough surfaces were produced, see part 3.4 of this paper. This indicates that the growth obstruction of ZnONRs by neighboring ones is strongest at these values of the synthesizing parameter. It is due to the combined effect of the specific Zn^{2+} concentration of the growth solution and related diameter of the SSW [23].

3.3. XRD and FT-IR spectra of the ZnONRs on 1[#]-3[#] SSW sieves

Fig. 5 illustrates the XRD spectra of the ZnONRs coated on SSW sieves in Fig. 3. At lower Zn^{2+} concentration of the growth solution, all seven peaks of the ZnONRs are indexed within 2θ range of $20°$ to $80°$, and their strengths are coarsely the same. This indicates that the orientation of the ZnONRs is quite random. When Zn^{2+} concentration of the growth solution increases, the strengths of (002) peaks become stronger whilst the others are still weak. It suggests that the ZnONRs gradually become well aligned and perpendicular to the cylindrical surfaces of the SSWs.

Moreover, Fig. 5a also exhibits that in comparison with other peak strengths, the (002) one of the ZnONRs synthesized at Zn^{2+} concentration 100 mM of the growth solution is the strongest. This means that the orientation of these ZnONRs on 1[#] SSW

sieve is better aligned, referring to Fig. 3a4. Similarly Fig. 5b and c demonstrates that the orientation of the ZnONRs synthesized respectively at Zn^{2+} concentration 75 and 50 mM of the growth solution on 2[#] and 3[#] SSW sieves is more desirable, see Fig. 3b3 and c2. As mentioned in Section 3.2, not only synthesizing parameters of ZnONRs but also the diameters of SSWs account for these differences of the XRD spectra.

Fig. 6 illustrates the FT-IR spectra of the ZnONRs in Fig. 3a2-a4, b2-b4, and c2-c4. Of all FT-IR spectra, the main absorption bands are at 470–530 cm^{-1}, 1380–1400 and 1600–1650 cm^{-1}, 2900–3000 cm^{-1}, and 3400–3500cm^{-1}, which represent the stretching mode of ZnO, the asymmetric and symmetric C=O stretching modes of zinc acetate, C-H mode, and O–H modes respectively. Fig. 6a shows that the transmittance at absorption band 3400–3500cm^{-1} of the ZnONRs in Fig. 3a4 is the least. This indicates that the quantity of hydroxyl radicals attached at the end faces of the ZnONRs in Fig. 3a4 are the most. Similarly Fig. 6b and c shows that the quantities of hydroxyl radicals attached at the top ends of the ZnONRs in Fig. 3b3 and c2 are the maximums respectively. This is due to the most numbers of defective sites, that is, the oxygen vacancies at the top ends of the ZnONRs [24]. It strongly suggests that the larger the diameter of a ZnONR is, the more the defective sites and further the hydroxyl radicals at the top end of the ZnONR are.

3.4. Quantitative characterization of the surface morphologies of ZnONRs on 1[#]-3[#] SSWs

The red curve in Fig. 2c is the extracted profile of the 2[#] SSW-supported ZnONRs at front view. With the component of low spatial frequency fitted and

subtracted from the extracted profile, the curve of the surface morphology of high spatial frequency was derived, the characteristic parameters Ra, ζ, Sk, and Ku were determined, and the surface morphology of the 2[#] SSW-supported ZnONRs at front view is quantitatively characterized. Similarly the characteristic parameters of 1[#] and 3[#] SSW-supported ZnONRs at front view were also acquired, referring to Fig. 7.

Fig. 7a demonstrates that when Zn^{2+} concentration of the growth solution becomes larger, Ra values of 1[#]-3[#] SSW-supported ZnONRs all decrease gradually whilst ζ values slightly increase. It indicates that the surfaces of SSW-supported ZnONRs all gradually get smoother and a little more correlated. Moreover, the blue Ra curve is below the green one but approximately over the red one, whilst the blue ζ curve is coarsely over the green one but below the red one. It suggests that the surfaces of 1[#] SSW-supported ZnONRs are smoothest and most correlated whilst that of 3[#] ones are roughest and most random. As mentioned in Sections 3.2 and 3.3, synthesizing parameters of the ZnONRs and diameters of the SSWs account for these different surface morphologies of 1[#]-3[#] SSW-supported ZnONRs.

Fig. 7b exhibits that most Sk values of 1[#] SSW-supported ZnONRs are positive whilst that of 2[#] and 3[#] ones negative (the Sk value of a Gaussian random rough surface is 0). This suggests that the surfaces of 1[#] SSW-supported ZnONRs have more bumps whilst that of 2[#] and 3[#] ones have more pits. Fig. 7b also demonstrates that the red Ku curve is approximately larger than 3 whilst both the green and blue curves are slightly less than 3 (the Ku value of a Gaussian random rough surface is 3). It indicates that the fluctuation of the surface heights of 1[#] SSW-supported ZnONRs is

larger than that of both $2^{\#}$ and $3^{\#}$ ones. As mentioned above, it is ascribed to synthesizing parameters of the ZnONRs and diameters of the SSWs. More important, as for $1^{\#}$, $2^{\#}$, and $3^{\#}$ SSW-supported ZnONRs produced respectively at Zn^{2+} concentration 100, 75, and 50 mM of the growth solution, the *Sk* values approach to 0 whilst the *Ku* values are coarsely equal to 3. This suggests that these SSW-supported ZnONRs all have Gaussian random rough surfaces, which is in agreement with the conclusions drawn from SEM micrographs in Section 3.2 as well as XRD patterns and FT-IR spectra in Section 3.3.

3.5. *Wettability of $1^{\#}$-$3^{\#}$ SSW sieve-supported ZnONRs*

Fig. 8a-c exhibits that when Zn^{2+} concentration of the growth solution increases, the CAs of $1^{\#}$-$3^{\#}$ ZnONR-deposited SSW sieves all decrease first, then reach the lowest point, and finally increase. This indicates that $1^{\#}$-$3^{\#}$ SSW sieve-supported ZnONRs undergo a similar wettability trend, that is, hydrophobic first, then most hydrophilic, and eventually hydrophobic again. It is ascribed to the transition between Cassie–Baxter and Wenzel regimes occurring on both ZnONR-deposited SSW sieves and SSW-supported ZnONRs, and more importantly, the former transition triggered by the latter one. For instance, when Zn^{2+} concentration of the growth solution increases, successively non-Gaussian, Gaussian, and non-Gaussian rough surfaces are formed on the SSW-supported ZnONRs. This gives rise to Cassie–Baxter to Wenzel regime transition first, and then Wenzel to Cassie–Baxter one. Once an aforementioned regime transition occurs on SSW-supported ZnONRs, it triggers similar regime transition on the corresponding ZnONR-deposited SSW sieve, which

15

eventually results in hydrophobic to hydrophilic or hydrophobic to hydrophobic transition. Fig. 8a-c also shows that the CA curve of 2[#] SSW sieve-supported ZnONRs is leading than that of 1[#] ones but lagging than that of 3[#] ones. This is due to the combined effects of the surface morphologies of the ZnONR-deposited SSWs and the meshes of the related SSW sieves. That is, the transition between Cassie–Baxter and Wenzel regimes is modulated by the synthesizing parameter of ZnONRs, the diameter of the SSW, and the mesh of the SSW sieve. More obviously, the Zn^{2+} concentration of the growth solution at which the most hydrophilic 1[#] SSW sieve-supported ZnONRs was produced is determined to be 100 mM, whilst that of the 2[#] and the 3[#] ones are to be 75 and 50 mM. Besides appropriate meshes of the related SSW sieves, Gaussian rough surfaces of the 1[#]-3[#] SSW-supported ZnONRs account for the knee points of these CA curves, referring to Fig. 7b.

3.6. Different photo-catalytic degradation of MB solution by 1[#]-3[#] SSW sieve-supported ZnONRs

Fig. 9a exhibits that the larger the concentration of MB solution, the stronger the absorbance. Moreover, the inset illustrates that the former variable is linear with the latter one, thus the former variable can be determined with the latter one. The photo-degradation mechanism of MB by ZnONRs via UV irradiation is as follows. When ZnONR-deposited SSW sieves are immersed into MB solution, which is irradiated by UV light with energy of *hv* equal to or larger than the band gap energy of ZnONR, electrons are excited from the valance band into the conduct one, leaving same amount of holes behind in the former band [24]. These holes act as powerful

16

oxidants for water molecules and react with hydroxyl groups to produce active hydroxyl radicals, whilst the electrons function as good reductants for molecular oxygens to generate the superoxides and further through a series of chemical reactions to produce additional active hydroxyl radicals. As strong oxidants these hydroxyl radicals diffuse into MB solution and effectively mineralize MB, and then the photo-degradation of this organic pollutant is complete.

Fig. 9b exhibits that when Zn^{2+} concentration of the growth solution goes up, the photo-degradation efficiencies of MB solution by $1^{\#}$-$3^{\#}$ ZnONR-deposited SSW sieves first increase gradually, then reach the highest points, and finally decrease slightly. Apparently, these photo-degradation curves undergo contrary trends to related CA curves in Fig. 8a-c. That is, the more hydrophilic a ZnONR-deposited SSW sieve is, the higher the photo-degradation efficiency of MB solution. In addition, according to the knee points of the photo-degradation curves of $1^{\#}$-$3^{\#}$ ZnONR-deposited SSW sieves, related Zn^{2+} concentration of the growth solution is determined to be 100, 75, and 50 mM, which exactly correspond to the ones at which the most hydrophilic SSW sieve-supported ZnONRs were produced respectively, referring to Fig. 8a-c.

As mentioned in Sections 3.4 and 3.5, synthesizing parameters of ZnONRs and diameters of $1^{\#}$-$3^{\#}$ SSWs determine the surface morphologies of related SSW-supported ZnONRs, which along with the mesh sizes of related SSW sieves further decide the wettability of the ZnONR-deposited SSW sieves. The more hydrophilic the surface of the ZnONR-deposited SSW sieve is, the larger the contacting surface area of the interface between the MB solution and the active crystal

plane (001) of the catalysts is, thus with UV irradiation the larger the throughput of active hydroxyl radicals is, and eventually the higher the photo-degradation efficiencies of MB solution by these SSW sieve-supported ZnONRs is. As for $1^{\#}$-$3^{\#}$ ZnONR-deposited SSW sieves produced at Zn^{2+} concentration 100, 75, and 50 mM of the growth solution, they all have Gaussian rough surfaces, which give rise to the largest actual contacting surface areas of active crystal plane (001) of ZnONRs with MB solution respectively. Furthermore, the combined effect of the Gaussian rough surfaces and related mesh sizes lead to the most hydrophilic ZnONR-deposited SSW sieves, which significantly decreases the sizes of air bubbles trapped within the square screen openings and once again remarkably increases the actual contacting surface areas of active crystal plane (001) of ZnONRs with MB solution. In the end, via UV irradiation, the corresponding throughputs of active hydroxyl radicals by related $1^{\#}$-$3^{\#}$ ZnONR-deposited SSW sieves are the largest, thus the photo-degradation efficiencies of MB solution are the highest respectively.

4. Conclusions

With ZnONRs hydrothermally synthesized on SSW sieves of mesh 300, 200, 150 and Zn^{2+} concentration of the growth solution regulated, the ZnONR-based photo-reactors were batch fabricated. The line edges of the features of interest were extracted, and the surface morphologies of the SSW sieve-supported ZnONRs were quantitatively characterized. It concluded that not only the synthesizing parameters but also the diameters of the SSW affected significantly the nucleation density of ZnO seeds and the surface morphology of the SSW-supported ZnONRs. Further the

surface morphology of the SSW-supported ZnONRs together with the mesh size of the SSW sieve determined the wettability of the SSW sieve-supported ZnONRs and the total contacting surface area of (001) active crystal planes of ZnONRs with MB solution. Of all $1^{\#}$-$3^{\#}$ SSW sieve-supported ZnONRs, those produced at Zn^{2+} concentration 100, 75, and 50 mM of the growth solution all have Gaussian random rough surfaces and are most hydrophilic. Hence the actual contacting surface area of (001) active crystal planes of ZnONRs is the largest, the yield of hydroxyl radicals the highest, and thus the photo-catalytic degradation of MB the optimal. In addition, the characteristic parameters Sk and Ku affected more significantly the wettability and the photo-degradation efficiency of the SSW sieve-supported ZnONRs than Ra and ζ. The results can benefit the batch fabrication and the performance improvement of these ZnONR-based photo-reactors.

Acknowledgements

References

[1] Y. Xu, J. J. Jin, X. L. Li, Y. D. Han, H. Meng, T. Y. Wang, X Zhang, Mater. Res. Bull. 76

(2016) 235–239.

[2] Y. J. Chiang, C. C. Lin, Powder Technol. 246 (2013) 137-143.

[3] S. Zargari, R. Rahimi, A. Ghaffarinejad, A. Morsali, J. Colloid Interface Sci. 466 (2016) 310-321.

[4] L. Lin, H. Y. Wang, H. M. Luo, P. Xu, J. Photochem. Photobiol., A. 307 (2015) 88-98.

[5] T. T. Vu, L. del Río, T. Valdés-Solís, G. Marbán, J. Hazard. Mater. 246-247 (2013) 126-134.

[6] Z. Z. Han, L. Liao, Y. T. Wu, H. B. Pan, S. F. Shen, J. Z. Chen, J. Hazard. Mater. 217-218 (2012) 100-106.

[7] W. Bai, K. Yu, Q. X. Zhang, X. Zhu, D. Y. Peng, Z. Q. Zhu, N. Dai, Y. Sun, Physica E. 40 (2008) 822-827.

[8] Y. C. Chang, Catal. Commun. 56 (2014) 45-49.

[9] L. Kashinath, K. Namratha, K. Byrappa, Appl. Surf. Sci. 357 (2015) 1849-1856.

[10] M. Y. Lu, Y. T. Tseng, C. Y. Chiu, Nanoscale Research Letters. 9 (2014) 667-674.

[11] M. H. Hsu, C. J. Chang, J. Hazard. Mater. 278 (2014) 444-453.

[12] H. Abdullah, D. H. Kuo, Y. R. Kuo, F. A. Yu, K. B. Cheng, J. Phys. Chem. C, 120 (2016) 7144-7154.

[13] H. Lu, M. Zhang, M. Guo, Appl. Surf. Sci. 317 (2014) 672-681.

[14] T. T. Vu, L. del Río, T. Valdés-Solís, G. Marbán, Appl. Catal., B: Environmental. 140-141 (2013) 189-198.

[15] T. T. Vu, L. del Río, T. Valdés-Solís, G. Marbán, Mater. Res. Bull. 47 (2012) 1577-1586.

[16] S. Jung, K. Yong, Chem. Commun. 47 (2011) 2643–2645.

[17] G. Marbán, A. López, I. López, T. Valdés-Solís, Appl. Catal., B: Environmental. 99 (2010) 257-264.

[18] J. Zhang, W.X. Que, Q.Y. Jia, X.D. Ye, Y.C. Ding, Controllable hydrothermal synthesis of ZnO nanowires arrays on Al-doped ZnO seed layer and patterning of ZnO nanowires arrays via surface modification of substrate, Appl. Surf. Sci. 257 (2011) 10134.

[19] C.J. Campbell, S.K. Smoukov, K.J.M. Bishop, E. Baker, B.A. Grzybowski, Direct printing of 3D and curvilinear micrometer-sized architectures into solid substrates with sub-micrometer resolution, Adv. Mater. 18 (2006) 2004.

[20] C. Li, G.S. Hong, P.W. Wang, D.P. Yu, L.M. Qi, Wet chemical approaches to patterned arrays of well-aligned ZnO nanopillars assisted by monolayer colloidal crystals, Chem. Mater. 21(2009) 891.

[21] C. S. Liu, Y. Masuda, Z. W. Li, Q. Zhang, T. Li, Site-selective growth of highly oriented ZnO rod arrays on patterned functionalized Si substrates from aqueous solution, Cryst. Growth Des. 5 (2009) 2168.

[22] Y. P. Zhao, G. C. Wang, T. M. Lu, Characterization of Amorphous and Crystalline Rough Surface: Principles and Applications. Academic Press, New York, 2001.

[23] W. X. Jing, H. Qi, J. F. Shi, Z. D. Jiang, F. Zhou, Y. Y. Cheng, K. Gao, Appl. Surf. Sci. 355 (2015) 403–410.

[24] J. H. Zeng, B. B. Jin, Y. F. Wang, Chem. Phys. Lett. 472 (2009) 90-95.

[25] Z. T. Han, J. J. Li, W. T. He, S. S. Li, Z. Li, J. K. Chu, Y. Chen, Microelectron. Eng. 111 (2013) 199-203.

Figure captions

Fig. 1. The SSWs of $1^{\#}$-$3^{\#}$ sieves (top right insets) with mesh 300 (a), 200 (b), and 150

(c) respectively.
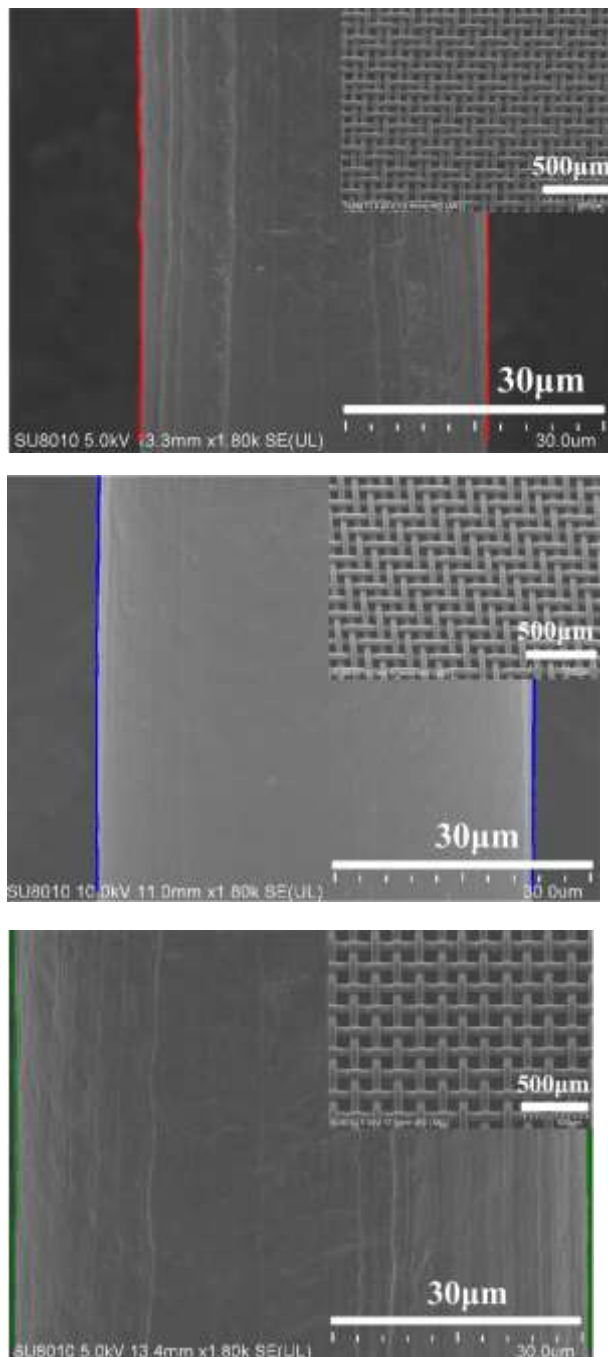
Fig. 2. A ZnONR-deposited SSW sieve of mesh 200 (a), the SSW-supported ZnONRs at front view (b), the partial SSW-supported ZnONRs at front and side view (c and the bottom left inset), and the detailed ZnONRs on the SSW (d). The ZnONRs were synthesized with Zn^{2+} concentration of the seed solution and the growth solution, the growth duration, and the growth temperature as 1 mM, 75 mM, 2.5 h, and $90^{o}C$ respectively.

SU8010 10.0kV 9.8mm x60.0k SE(UL)

500nm

500nm
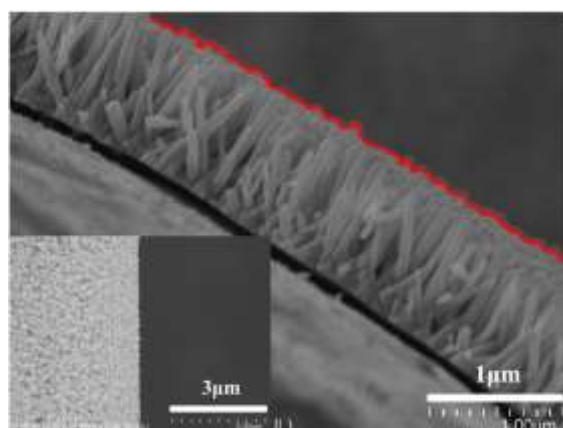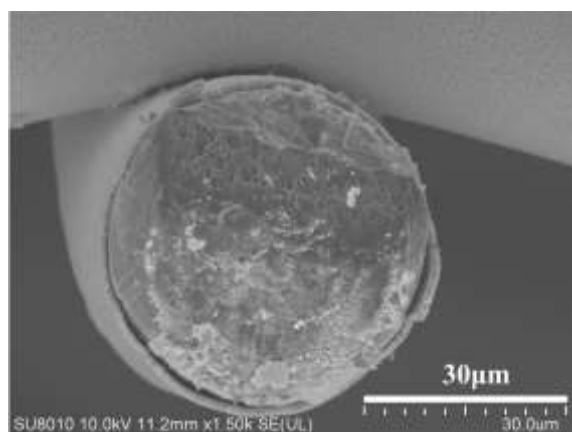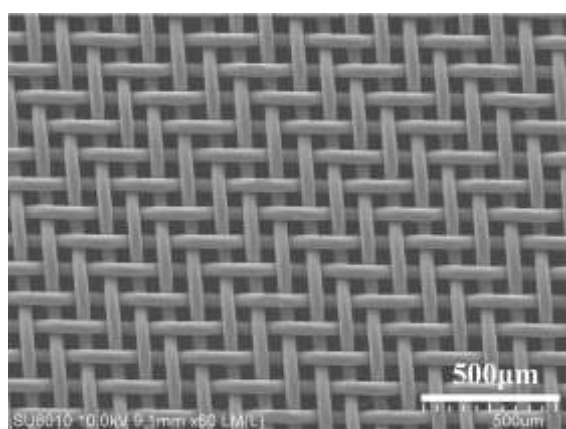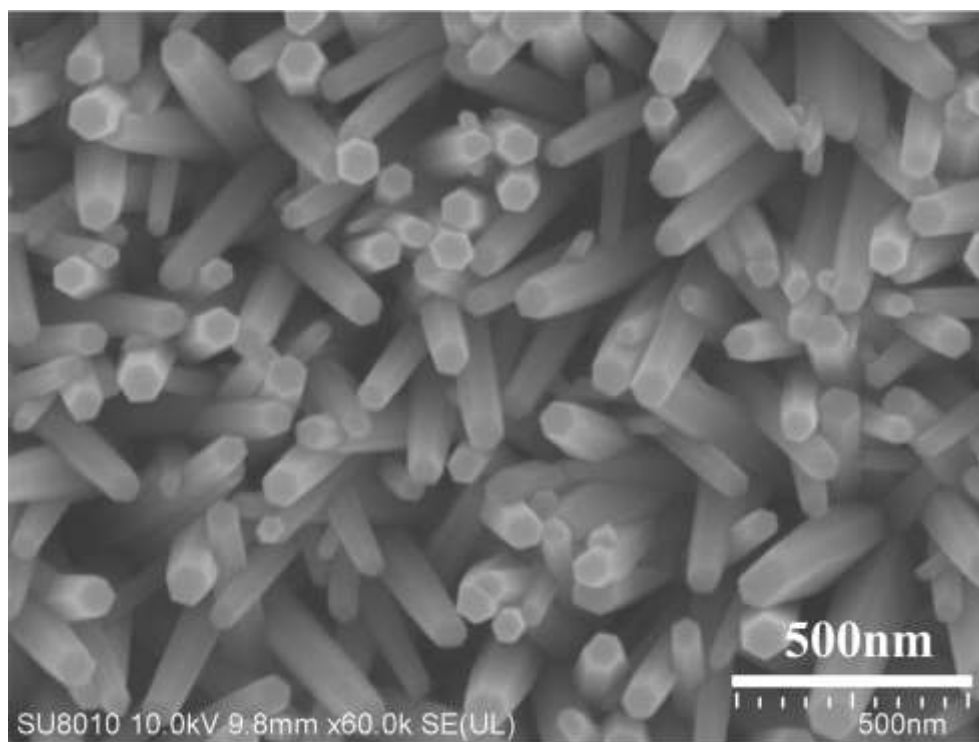
Fig. 3. Detailed ZnONRs synthesized at Zn^{2+} concentration 25 (a1, b1, c1), 50 (a2, b2, c2), 75 (a3, b3, c3), 100 (a4, b4, c4), and 125 (a5, b5, c5) mM of the growth solution on $1^{\#}$ (a1-5), $2^{\#}$ (b1-5), $3^{\#}$ (c1-5) SSW sieves, whilst Zn^{2+} concentration of the seed solution, the growth duration and the growth temperature were 1 mM, 2.5 h, and $90^{o}C$.
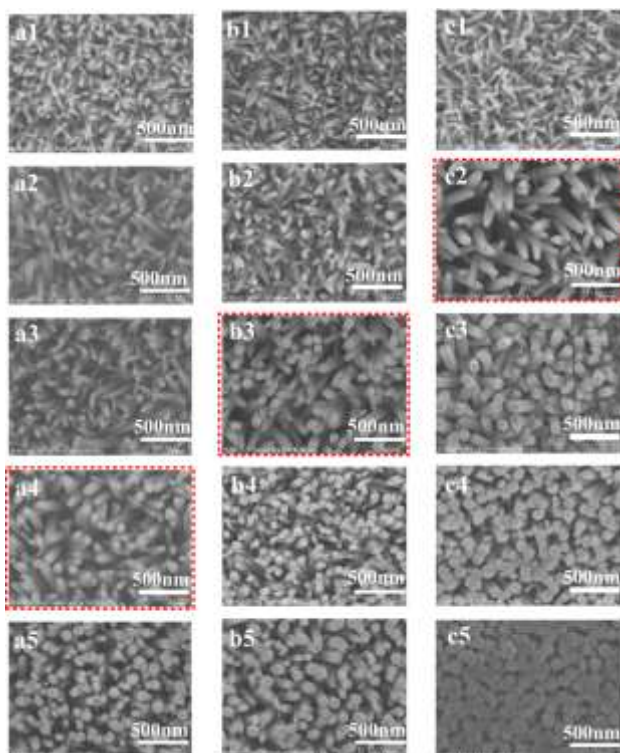
Fig. 4. Densities of ZnONRs synthesized at different Zn^{2+} concentration of the growth solution on 1[#], 2[#], and 3[#] SSW sieves (ZnONRs are the same as that shown in Fig. 3 in the revised manuscript). Dashed lines represent for the density averages of ZnONRs on 1[#], 2[#], and 3[#] SSW sieves.
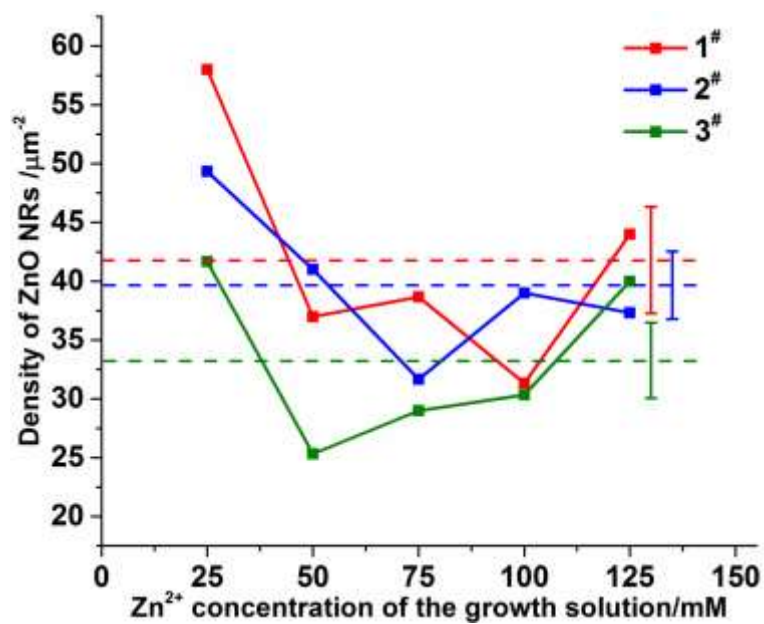
Fig. 5. XRD patterns of the ZnONRs on 1# (a), 2# (b), and 3# (c) SSW sieves.
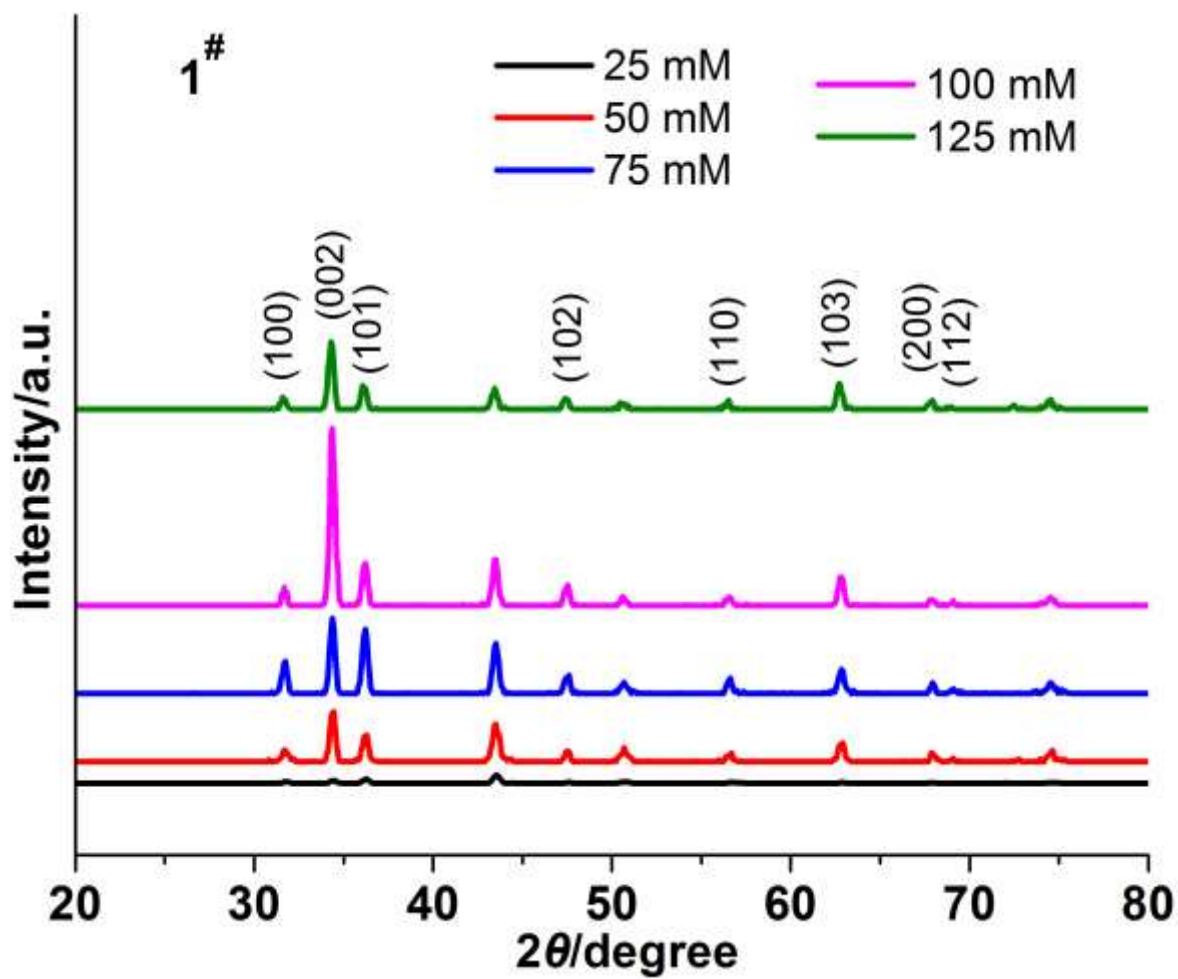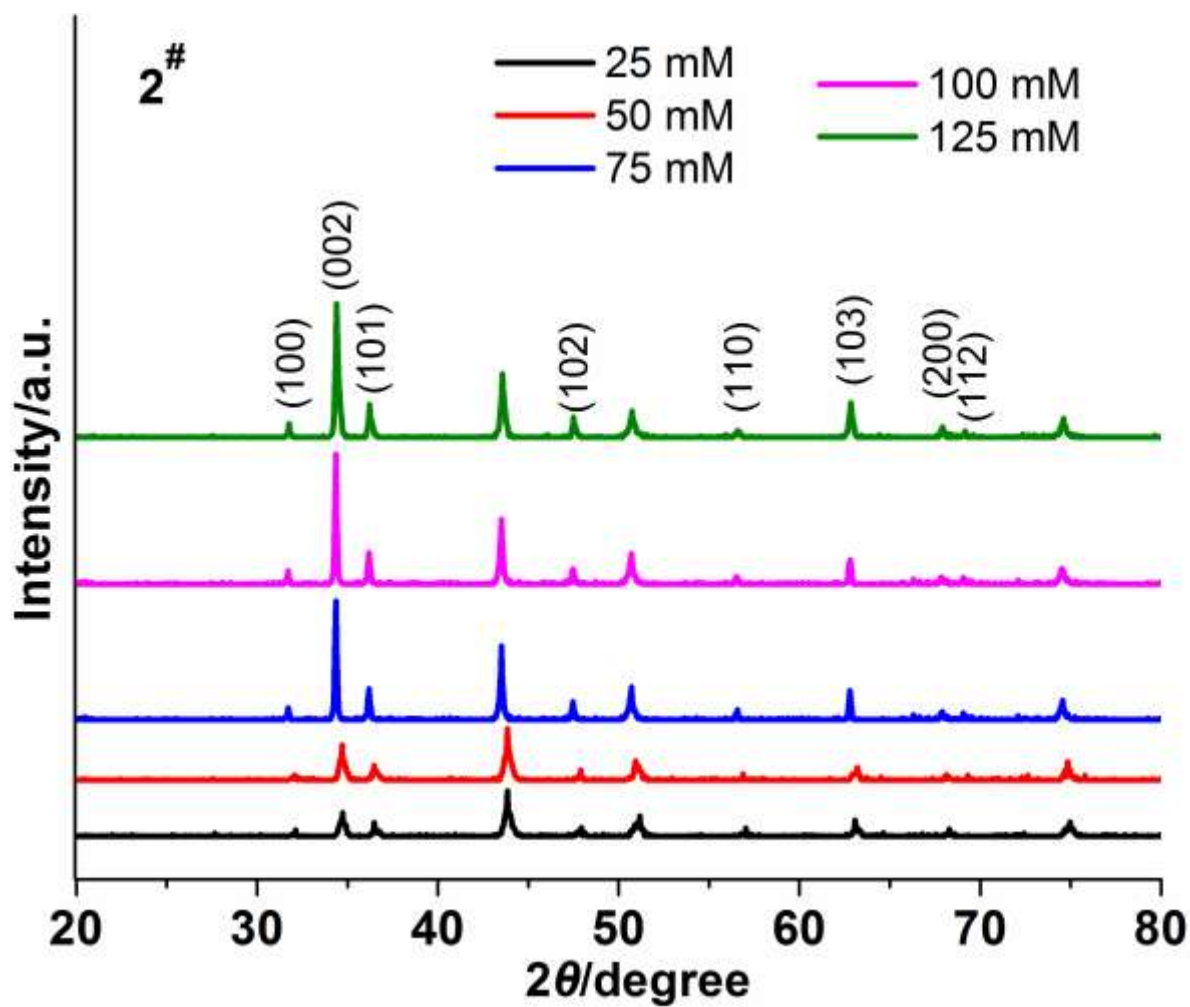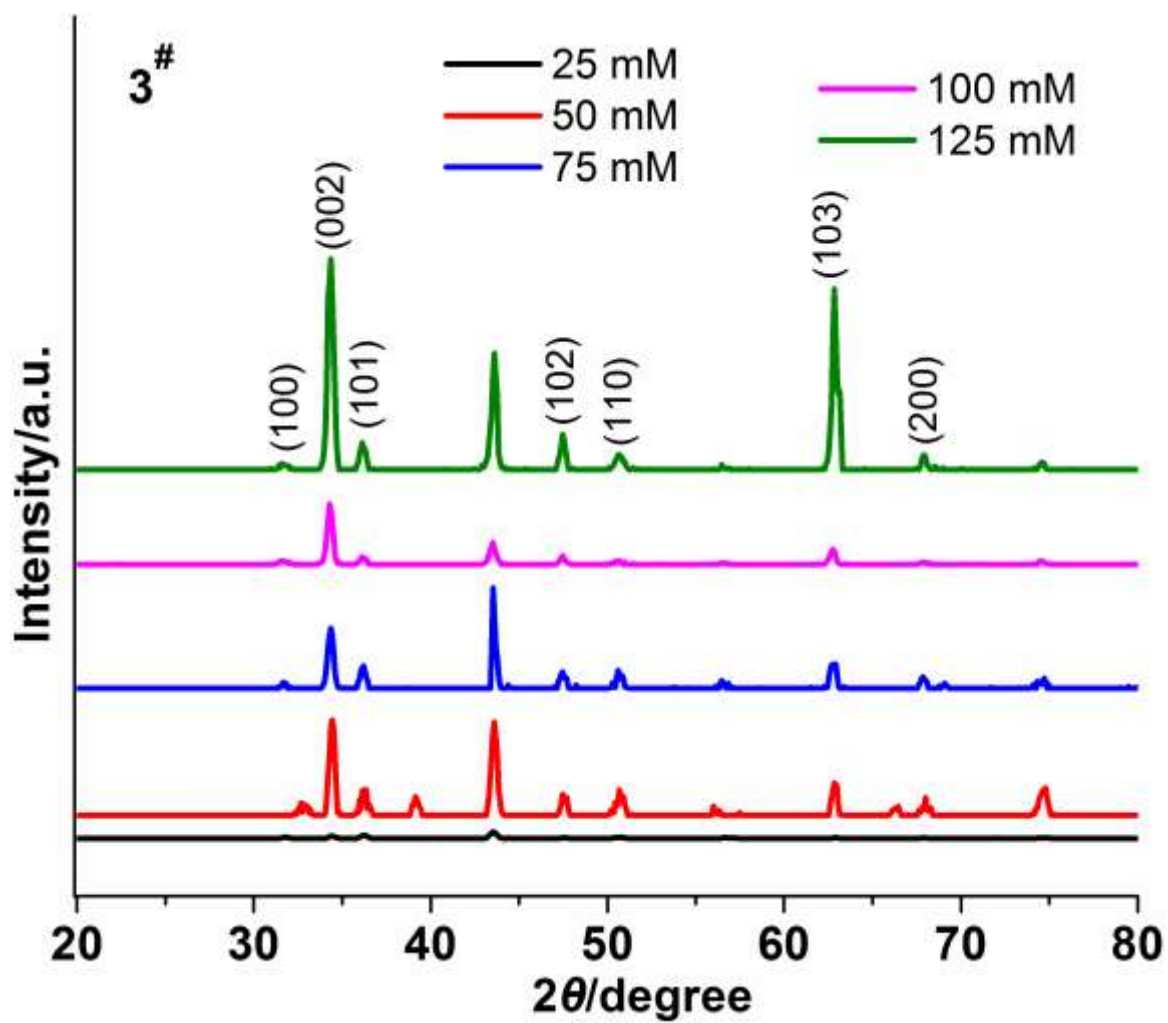
Fig. 6. FT-IR patterns of the ZnONRs synthesized at Zn^{2+} concentration 50, 75, and 100 mM of the growth solution on $1^{\#}$ (a), $2^{\#}$ (b), and $3^{\#}$ (c) SSW sieves.
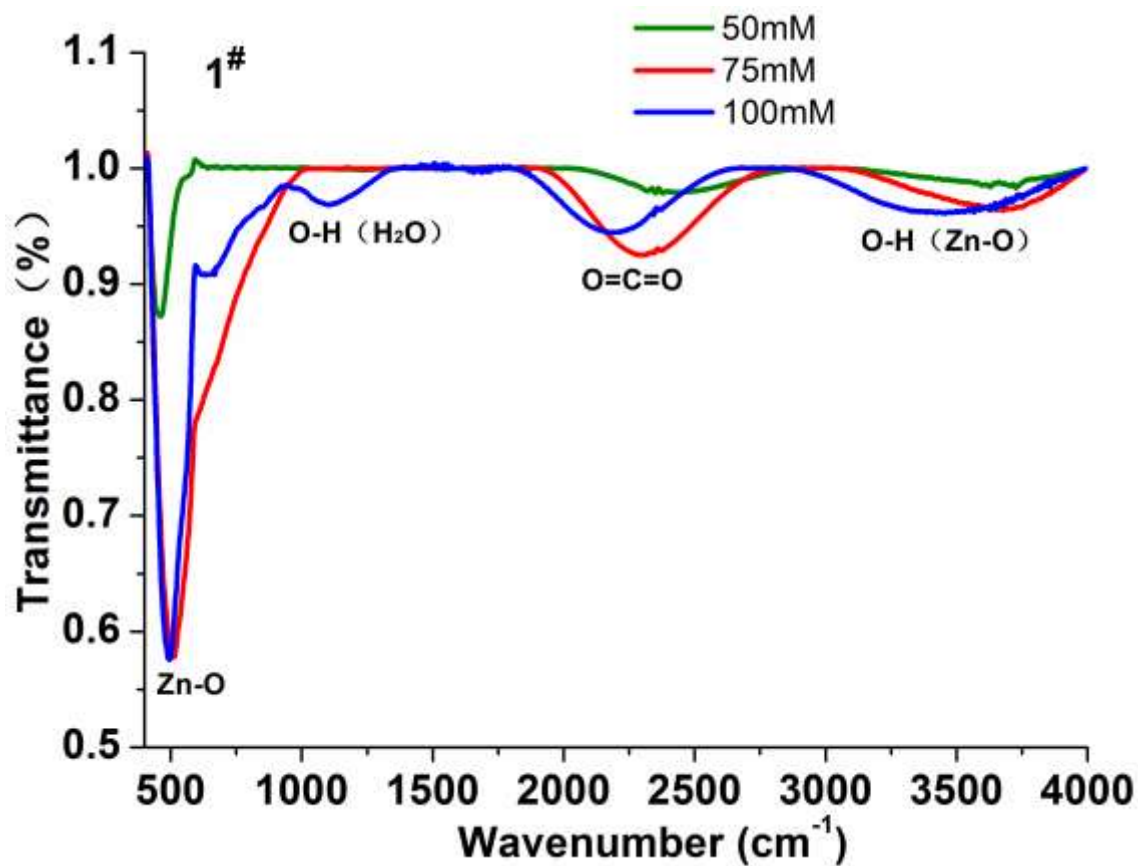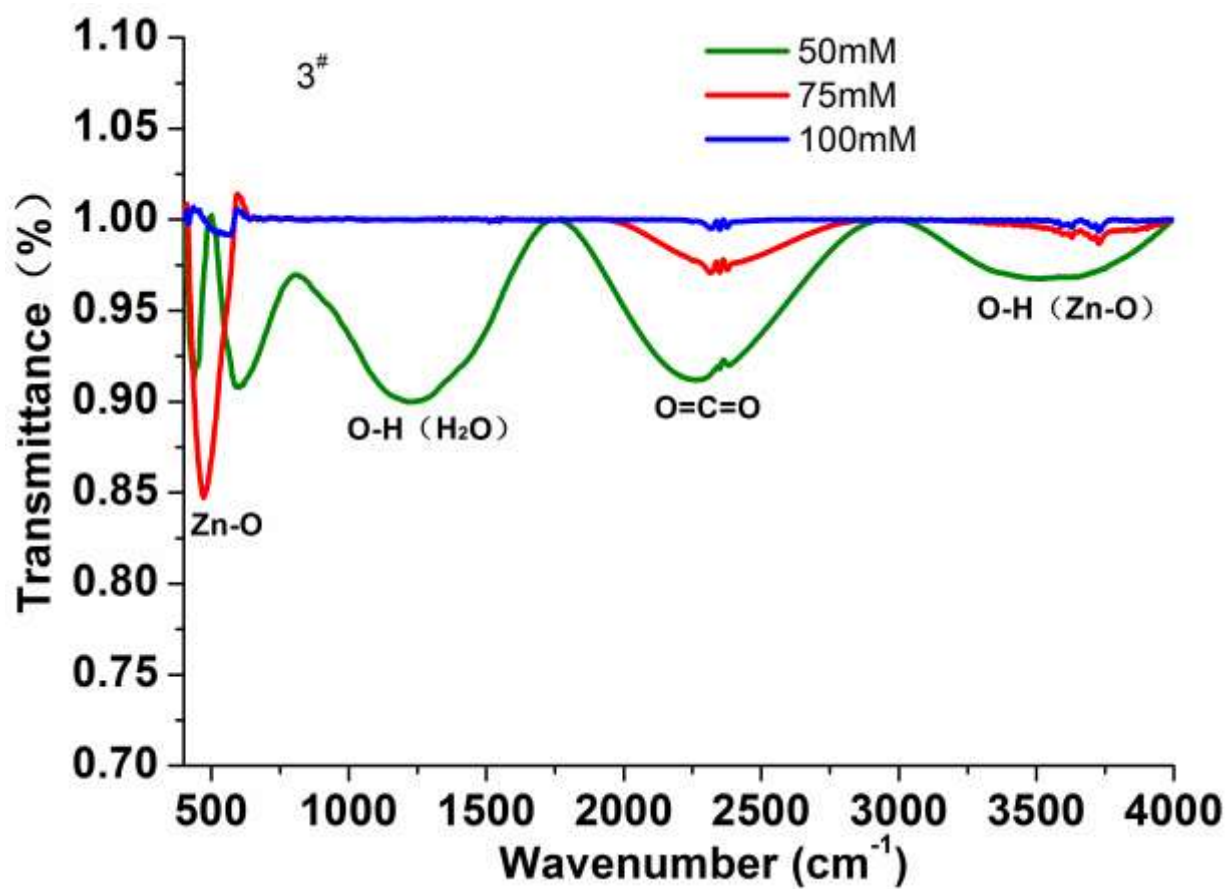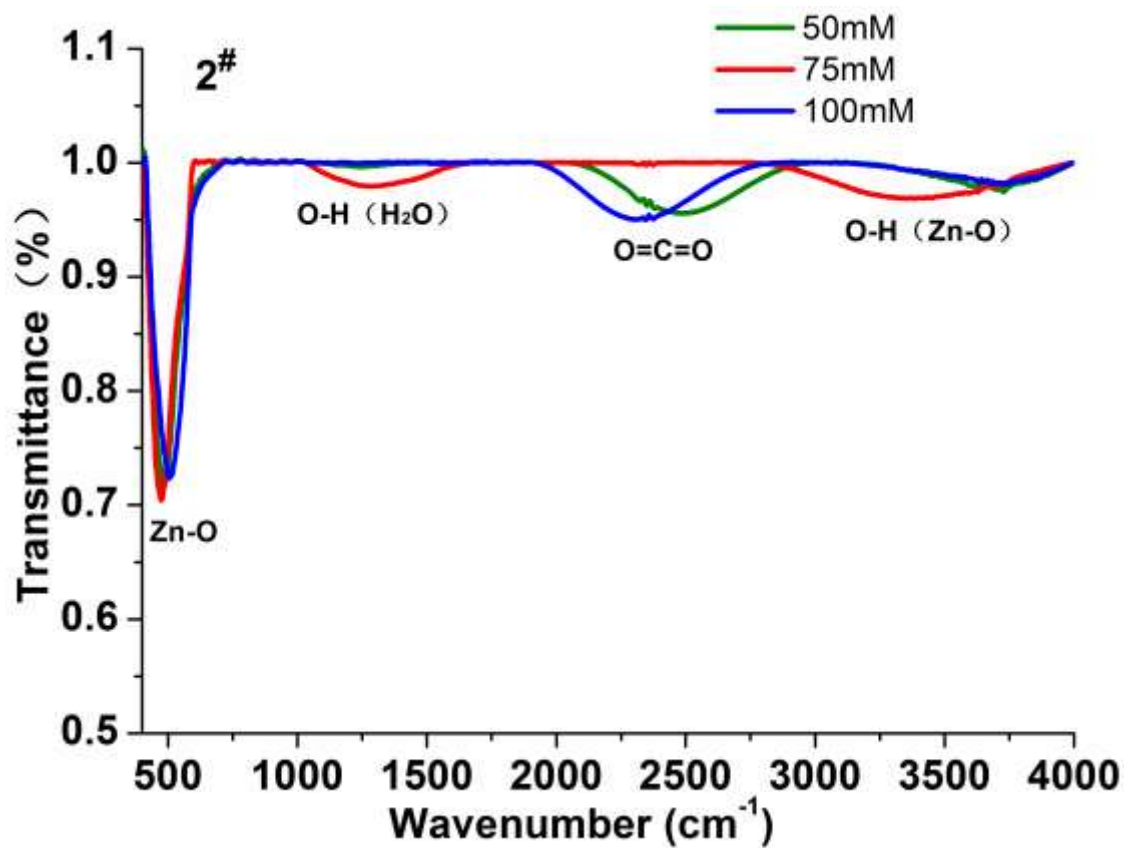
Fig. 7. Effects of Zn^{2+} concentration of the growth solution on the surface morphologies of $1^{\#}$-$3^{\#}$ SSW-supported ZnONRs. (a) *Ra* and *ζ*. (b) *Sk* and *Ku*.
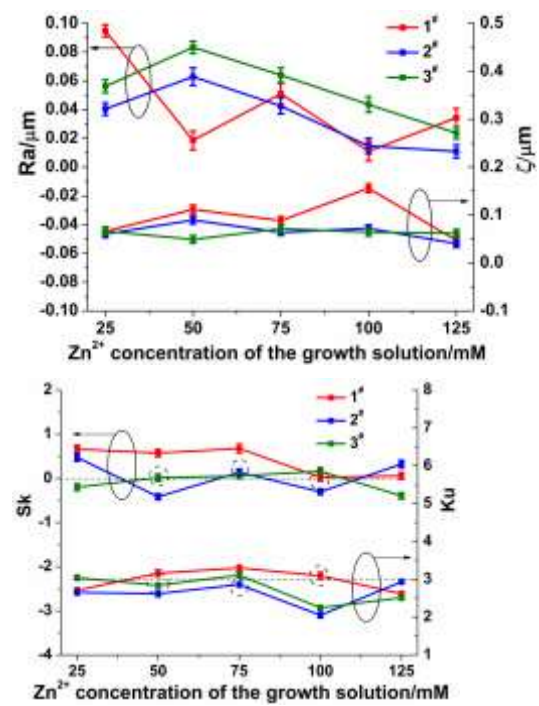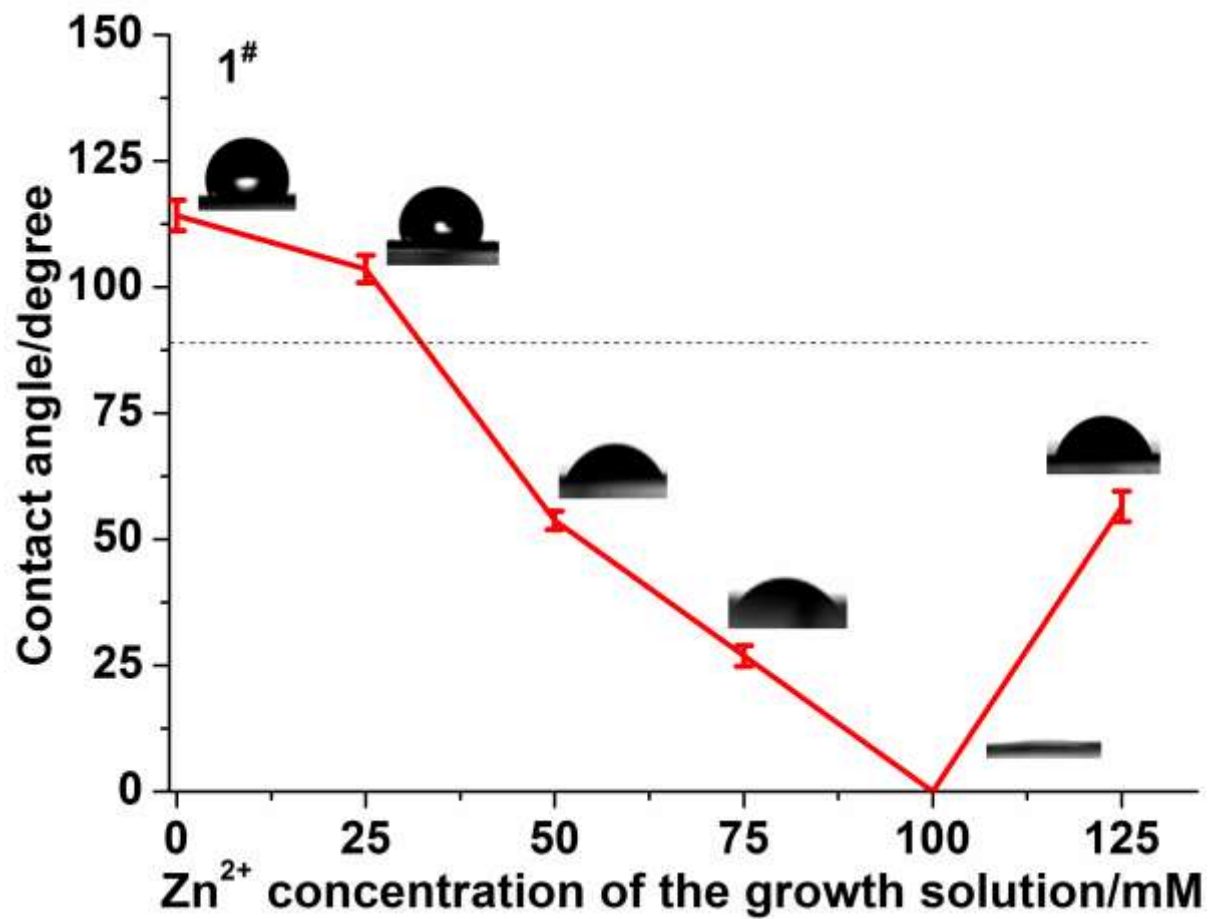
Fig. 8. Effects of Zn^{2+} concentration of the growth solution on the CAs of 1[#] (a), 2[#] (b),
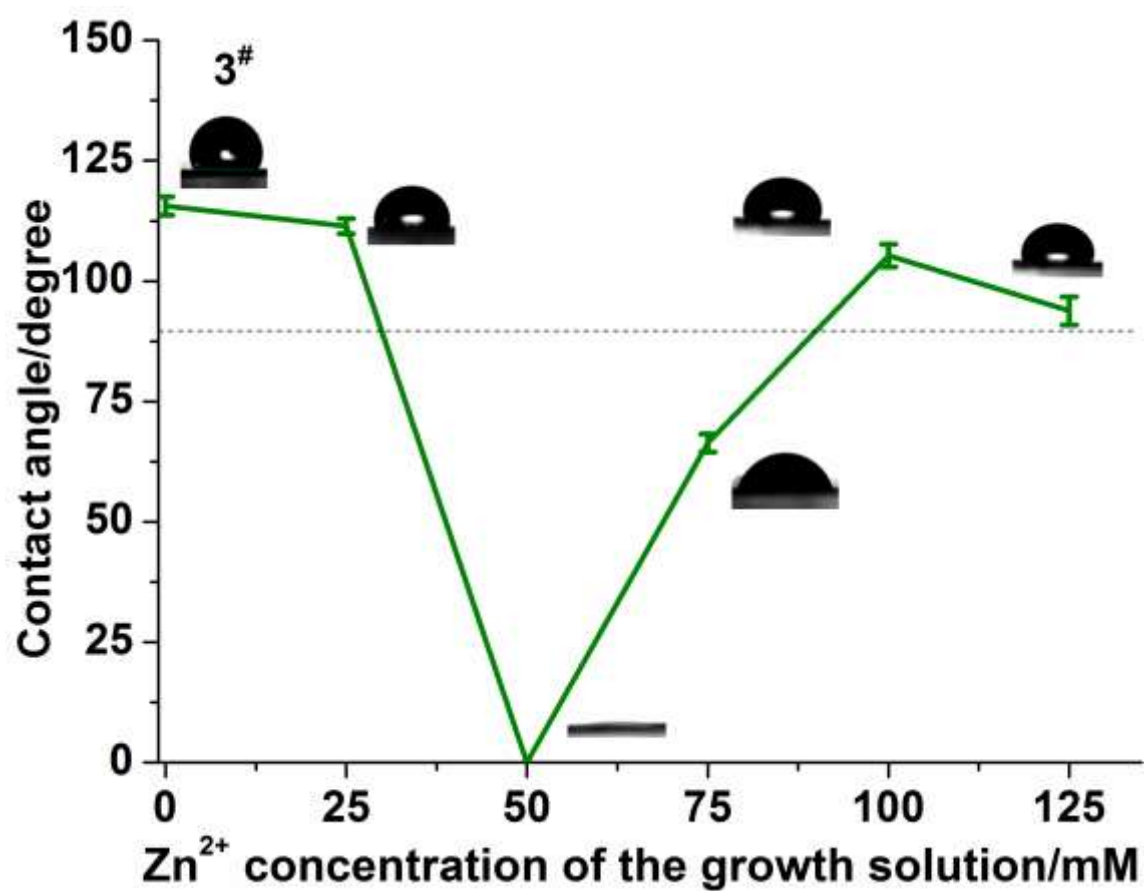
and 3[#] (c) SSW sieve-supported ZnONRs.
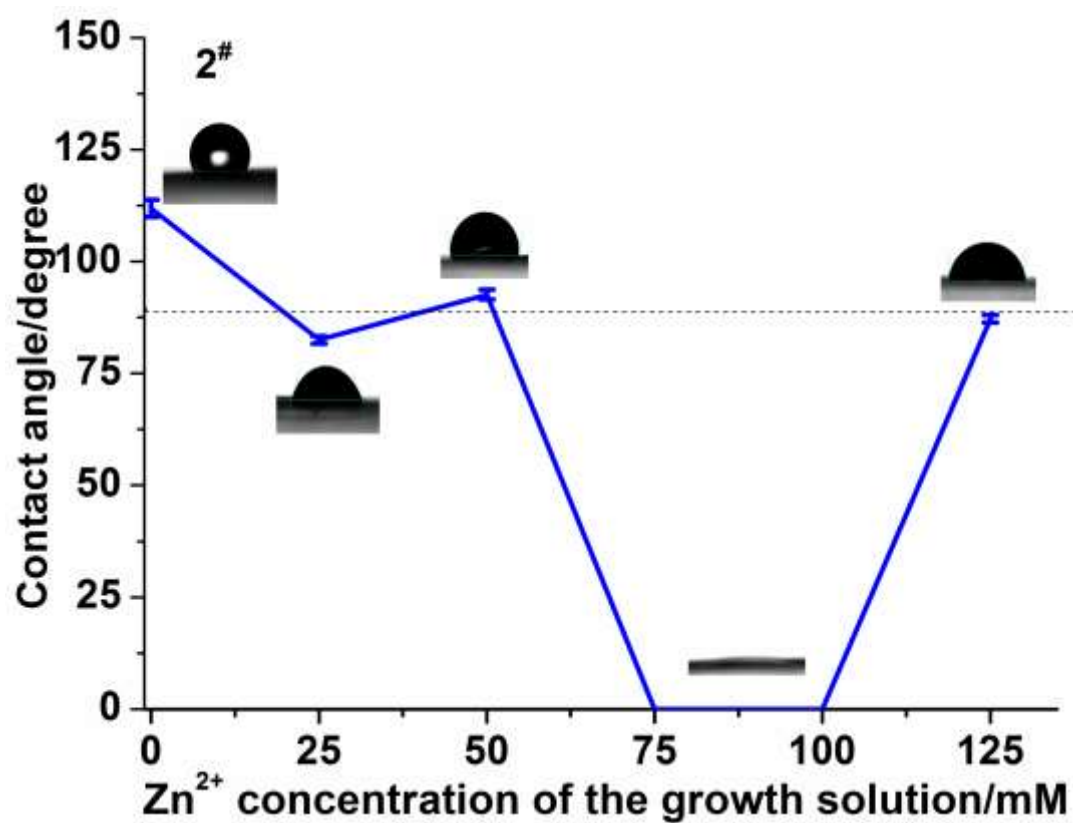
Fig. 9. The relationship between the concentration and the absorbance of MB solution (a), and different photo-degradation of MB by $1^{\#}$-$3^{\#}$ SSW sieve-supported ZnONRs synthesized at different Zn^{2+} concentration of the growth solution respectively (b).